

Upper critical fields and thermally-activated transport of Nd(O_{0.7}F_{0.3})FeAs single crystal.

J. Jaroszynski, F. Hunte, L. Balicas, Youn-jung Jo, I. Raičević, A. Gurevich, D. C. Larbalestier
National High Magnetic Field Laboratory, Florida State University, Tallahassee, Florida 32310, USA

F. F. Balakirev

National High Magnetic Field Laboratory, Los Alamos National Laboratory, Los Alamos, New Mexico 87545, USA

L. Fang, P. Cheng, Y. Jia and H. H. Wen

Institute of Physics, Chinese Academy of Sciences, Beijing 100190, People's Republic of China

(Dated: November 2, 2018)

We present detailed measurements of the longitudinal resistivity $\rho_{xx}(T, H)$, and the upper critical field H_{c2} of Nd(O_{0.7}F_{0.3})FeAs single crystals in strong DC and pulsed magnetic fields up to 45 T and 60 T, respectively. We found that the field scale of H_{c2} is comparable to $H_{c2} \sim 100$ T of high T_c cuprates. $H_{c2}(T)$ parallel to the c -axis exhibits a pronounced upward curvature similar to what was extracted from earlier measurements on polycrystalline La(O,F)FeAs, Nd(O,F)FeAs and Sm(O,F)FeAs samples. Thus this behavior of $H_{c2}(T)$ is indeed an intrinsic feature of oxypnictides, rather than manifestation of vortex lattice melting or granularity. The orientational dependence of $H_{c2}(\theta)$ as a function of the angle θ between \mathbf{H} and the c -axis shows deviations from the one-band Ginzburg-Landau scaling. The mass anisotropy parameter $\gamma(T) = (m_c/m_{ab})^{1/2} = H_{c2}^{\parallel}/H_{c2}^{\perp}$ obtained from these measurements decreases as temperature decreases, from $\gamma \simeq 9.2$ at 44 K to $\gamma \simeq 5$ at 34 K, where \parallel and \perp correspond to \mathbf{H} parallel and perpendicular to the ab planes, respectively. Spin dependent magnetoresistance and nonlinearities in the Hall coefficient suggest contribution to the conductivity from electron-electron interactions modified by disorder reminiscent that of diluted magnetic semiconductors. The Ohmic resistivity $\rho_{xx}(T, H)$ measured below T_c but above the irreversibility field exhibits a clear Arrhenius thermally activated behavior $\rho = \rho_0 \exp[-E_a(T, H)/T]$ over 4 – 5 decades of ρ_{xx} . The activation energy $E_a(T, H)$ has very different field dependencies for $\mathbf{H} \parallel \mathbf{ab}$ and $\mathbf{H} \perp \mathbf{ab}$, varying from 4×10^3 K at $H = 0.2$ T to ~ 200 K at $H = 35$ T. We discuss to what extent different pairing scenarios suggested in the literature can manifest themselves in the observed behavior of H_{c2} , using the two-band model of superconductivity in oxypnictides. The results indicate the importance of paramagnetic effects on $H_{c2}(T)$ in oxypnictides, which may significantly reduce $H_{c2}(0)$ as compared to $H_{c2}(0) \sim 200 - 300$ T based on extrapolations of $H_{c2}(T)$ near T_c down to low temperatures.

PACS numbers: 74.70.-b, 74.25.Fy, 74.72.-h, 74.81.Bd

The recently discovered layered superconducting oxypnictides with high transition temperatures T_c^1 are based on alternating structures of FeAs layers and REO layers of rare earth (RE) oxides. Similar to the high-temperature superconducting cuprates, superconductivity in oxypnictides emerges upon doping of a parent antiferromagnetic state. As the REO planes are doped, the ionically bonded REO donates an electron to the covalently bonded FeAs plane², suppressing the global antiferromagnetism and resulting in superconductivity.

Previous low field^{3,4,5,6} and high field transport studies^{7,8} on different polycrystalline oxypnictides have shown, that their magneto-transport behavior is intermediate between conventional low- T_c superconductors and the high-temperature cuprates. However, while La(O,F)FeAs behaves as an intermediate- T_c superconductor similar to MgB₂ in which thermal fluctuations of vortices do not significantly affect the H - T diagram to the extent that they do in the layered cuprates, the higher T_c oxypnictides like SmFeAsO_{0.85} and Nd(O,F)FeAs exhibit larger mass anisotropies, enhanced thermal fluctuations, and a Ginzburg parameter comparable to that

of YBCO. Thus, the question arises, whether this distinct behavior stems from different critical temperatures, the presence of magnetic ions^{9,10,11}, or is due to the electromagnetic granularity of these polycrystalline samples^{12,13,14}. For example, is the pronounced upward curvature of $H_{c2}(T)$ along the c -axis extracted from measurements of the resistivity onsets of polycrystals⁷ indeed an intrinsic feature of $H_{c2}^{\perp}(T)$ in oxypnictides, or does it reflect an extrinsic effect of magnetic granularity, the onset of the irreversible critical state behavior and/or melting of the vortex lattice? Moreover, given that the nature of superconductivity in the oxypnictides is still poorly understood, several different scenarios have been proposed. In particular, many theoretical models are based on the multiband electronic structure of the oxypnictides and the fact that the superconducting state emerges upon doping of the parent antiferromagnetic semimetal^{15,16,17,18,19}. The multiband effects would manifest themselves in the distinct temperature and orientational dependencies of $H_{c2}(T)$, as has been well documented in detailed studies of MgB₂^{20,21,22,23,24,25,26,27,28,29,30,31,32}. To address these

issues, we made detailed measurements of the magneto-transport properties of a $\text{Nd}(\text{O}_{0.7}\text{F}_{0.3})\text{FeAs}$ single crystal in very high magnetic fields.

I. SAMPLES

The crystal was made by the flux method using NaCl as the flux. First the starting Nd (purity 99.95 %) and As (purity 99.99 %) were mixed in 1:1 ratio, ground and pressed into a pellet shape. Then it was sealed in an evacuated quartz tube and reacted at 800 °C for 10 hours. The resultant pellet was ground together with a stoichiometric powder mixture of NdF_3 (purity 99.95 %), Fe_2O_3 (purity 99.9 %) and Fe (purity 99.9%) resulting in $\text{Nd}(\text{O}_{0.7}\text{F}_{0.3})\text{FeAs}$ compound. Again it was pressed into a pellet and put together with NaCl powder of mass ratio (NaCl : $\text{Nd}(\text{O},\text{F})\text{FeAs}$ = 10:1) and sealed in an evacuated quartz tube and reacted at about 1050 °C for 10 days. Then it was cooled down at a rate of 3 °C/hour to 850 °C, followed by a quick cooling to room temperature by shutting off the power of the furnace. The resulting product contains mainly plate-like small crystals with lateral dimensions of 5–50 μm and $\sim 1 \mu\text{m}$ thickness.

Previous extensive transport^{33,34,35} and heat capacity³⁶ studies on $\text{Nd}(\text{O}_{0.82}\text{F}_{0.18})\text{FeAs}$ single crystal revealed the onset of superconductivity at $T_c \approx 47$ K, the upper critical fields $H_{c2}^{\parallel}(0) = 304$ T and $H_{c2}^{\perp}(0) = 62 - 70$ T extrapolated from the Werthamer-Helfand-Hohenberg (WHH) formula³⁷. These samples also have a relatively small mass anisotropy parameter $\gamma = (m_c/m_a)^{1/2} \lesssim 5$ where m_a and m_c are the effective masses along the ab plane and the c-axis, respectively. However, the above studies were performed in magnetic fields not exceeding 9 T, where most of the multi-band effects would not manifest themselves in the $H_{c2}(T)$ curves.

II. RESISTIVE TRANSITIONS AND UPPER CRITICAL FIELDS

For our experiment we used three different high-field magnets at the National High Magnetic Field Laboratory (NHMFL): 35 T DC resistive and 45 T hybrid magnets at Florida State University and 65 T pulsed field magnet at Los Alamos National Laboratory. The inset to Fig. 1(a) shows the scanning electron micrograph of the $\text{Nd}(\text{O},\text{F})\text{FeAs}$ sample with six Pt contacts fabricated by the focused ion beam (FIB) technique. The distance between voltage contacts is $\sim 13 \mu\text{m}$, and the sample thickness is $\sim 1.4 \mu\text{m}$. The sample was glued to a conductive silicon substrate to ensure good thermalization during measurement, and to prevent electric charge build-up during the FIB procedure. The sample was placed on a rotating platform, which allows us to change its orientation with respect to the magnetic field *in situ*. The longitudinal resistivity ρ_{xx} and the Hall coefficient R_H in high

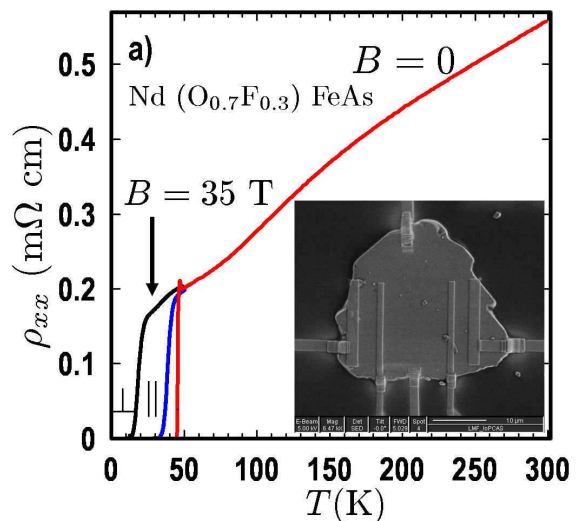


FIG. 1: Longitudinal resistivity $\rho_{xx}(T)$ at $H = 0$ and $H = 35$ T for $H \parallel ab$ and $H \perp ab$. At $B = 0$ superconductivity onset is observed at $T_c \approx 46$ K. Inset shows scanning electron micrograph of the sample.

magnetic fields were measured using a lock-in technique with AC excitation current below 0.3 mA at frequency 22 Hz. Pulsed field measurements were conducted using in-house synchronous digital lock-in technique at frequency of 16 kHz and similar levels of current.

Figure 1 shows $\rho_{xx}(T)$ as a function of temperature T at $H = 0$ and 35 T for different sample orientations. The magnetic field perpendicular to the ab plane shifts the superconducting transitions to lower T , reducing T_c (from 46 K to 21 K at $H = 35$ T) without significant change of the shape of $\rho_{xx}(T)$. This behavior is reminiscent of magnetotransport in low- T superconductors. In contrast, fields applied parallel to the ab plane change the shape of the resistive transitions more than they do for $H \parallel c$, but less than what was observed on polycrystalline $\text{Nd}(\text{O},\text{F})\text{FeAs}$ ⁸. Figure 1 shows that the $\rho_{xx}(T)$ dependence is sublinear at higher T but superlinear below $T \lesssim 100$ K. Over the same temperature range, the Hall resistivity $\rho_{xy}(T)$ shown in Fig. 2 has a relatively strong temperature dependence for such an optimally doped material. This dependence is much stronger than was observed on a polycrystalline sample with much lower doping, $x = 6 \%$ ⁸, with $\rho_{xy}(T)$ exhibiting a kink around $T \approx 100$ K. Such temperature dependencies of the transport coefficients near ~ 100 K may result from a multi-band conductivity or a structural transition. The inset to Fig. 2 shows $\rho_{xy}(H)$ at selected temperatures. On this field scale, $\rho_{xy}(H)$ does not exhibit field nonlinearities, at $40 < T < 300$ K, similarly to polycrystalline samples⁸. However, a strong dependence of $R_H(H)$ is observed in this single crystal at lower temperatures as will be discussed later.

Figures 3–6 show the detailed field and temperature dependencies of $\rho_{xx}(T, H)$, from which the upper crit-

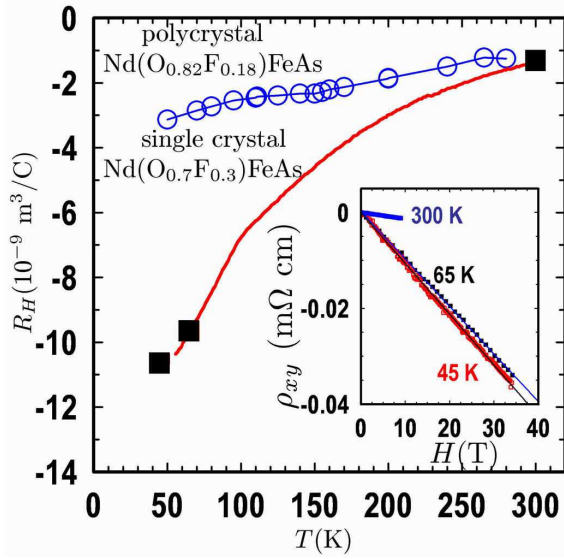


FIG. 2: Hall coefficient R_H as a function of T measured in superconducting magnet at ± 9 T (solid line), and determined from linear fits to $\rho_{xy}(H)$ for $-35 < H < 35$ T or $-9 < H < 9$ T (solid squares), as shown in the inset. R_H for polycrystalline $\text{Nd}(\text{O}_{0.94}\text{F}_{0.06})\text{FeAs}$ sample is also shown.

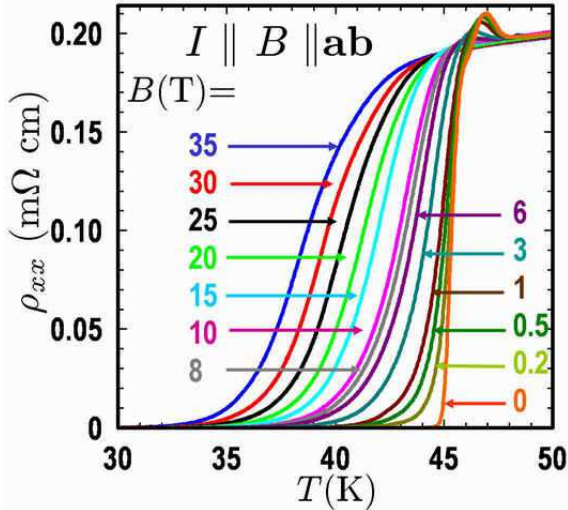


FIG. 3: ρ_{xx} as a function of temperature at various magnetic fields for $H \parallel ab$.

ical fields parallel and perpendicular to the ab planes were extracted. Here H_{c2} for both field orientations was measured at the onset of the superconductivity transition defined by the intersection point from linear extrapolations of $\rho_{xx}(T, H)$ at $T < T_c$ and $\rho_n(T, H)$ at $T > T_c$, as shown in Fig. 4. Here $\rho_n(T, H)$ is the resistivity in the normal state. We also extracted the mid transition field $H_{50}(T)$ and the resistivity onset fields $H_{10}(T)$ and $H_{0.5}(T)$ defined by $\rho_{xx}(T, H) = 0.5\rho_n(T, H)$, $\rho_{xx}(T, H) = 0.1\rho_n(T, H)$, and $\rho_{xx}(T, H) = 0.05\rho_n(T, H)$, respectively. The fields $H_{0.5}(T)$ are close

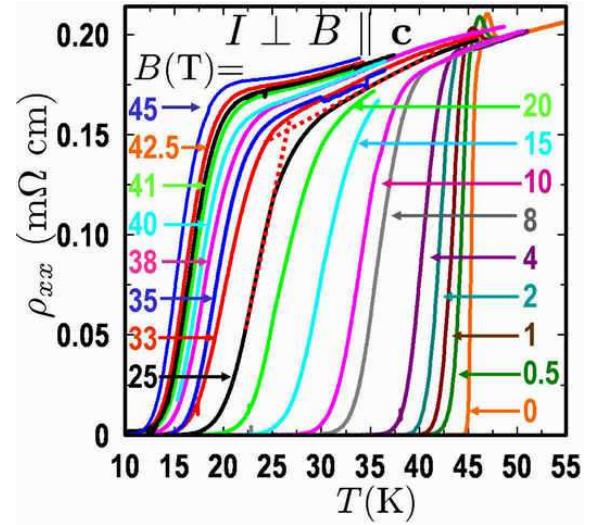


FIG. 4: ρ_{xx} as a function of temperature at various magnetic fields for $H \perp ab$. Dotted lines show how the onset of the transition was determined for $H = 20$ T. Excitation current $I \leq 0.3$ mA, at frequency $f = 22$ Hz was applied in the ab plane.

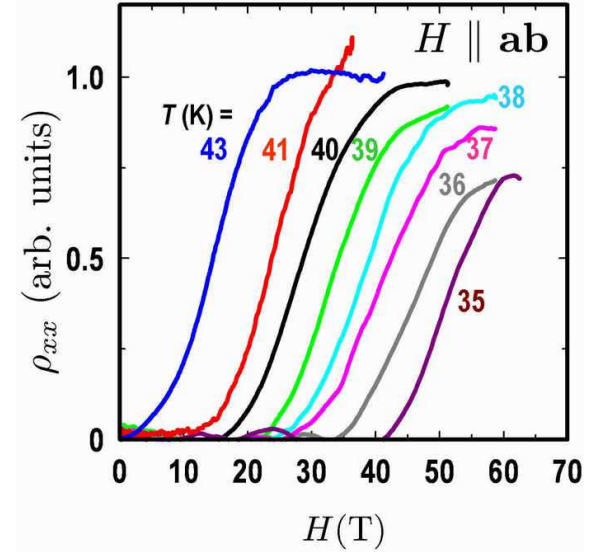


FIG. 5: The longitudinal resistivity $\rho_{xx}(H)$ as a function of magnetic field in for $H \parallel ab$ measured in pulsed magnet up to 60 T.

to the irreversibility field H^* , which quantifies the onset of vortex critical state. The resulting temperature dependencies of all these fields are summarized in Figs. 8 and 9. Notice that the $R(T)$ curves shown in Figs. 3–6 exhibit a small peak just before the transition which disappears at $H > 4$ T for $\mathbf{H} \parallel c$ and $H > 6$ T for $\mathbf{H} \parallel ab$. Such resistance peak anomaly has been observed in other superconductors and is usually ascribed to the effect of paramagnetic ions, sample inhomogeneities, contact arrangements, etc.^{38,39,40,41}. Since the mechanism of this

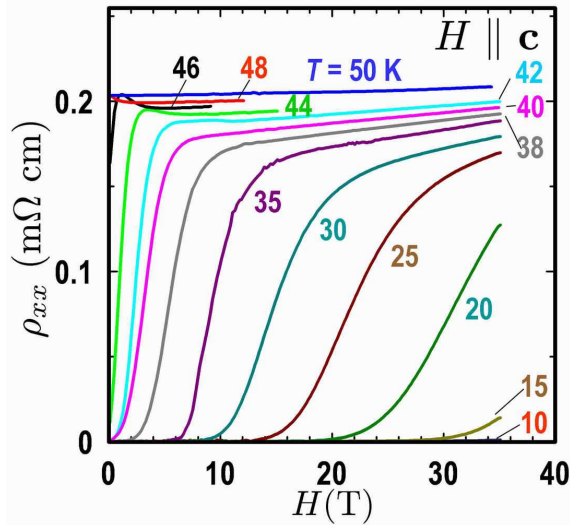


FIG. 6: The longitudinal resistivity $\rho_{xx}(H)$ as a function of magnetic field in for $H \perp ab$ measured in DC resistive magnet up to 35 T at various temperatures.

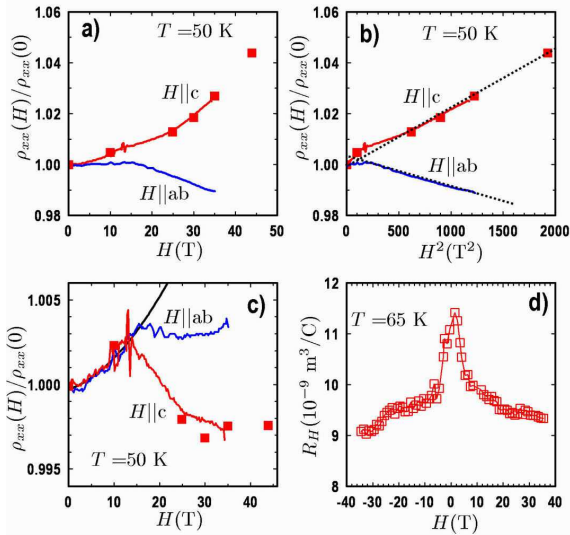


FIG. 7: Magnetoresistance measured at $T = 50$ K for two different sample configurations. Squares denote data from temperature sweeps at fixed magnetic field, while solid lines were measured at fixed T . (b) The same data plotted versus H^2 . Dotted lines show linear fits taken for $H \gtrsim 15$ T. (c) Data plotted after subtraction of the H^2 contribution. (d) Hall coefficient $R_H(H) = \rho_{xy}(H)/H$ versus magnetic field measured at $T = 65$ K.

anomaly is still not completely understood, we did not take it into account when extracting H_{c2} from the data shown in Figs. 3-6.

Figure 7(a) shows the magnetoresistance (MR) at $T = 50$ K, just above the onset of superconductivity. The MR is positive for $H||c$ and negative for $H||ab$. The difference could be attributed to orbital origin of this MR. As shown in Fig. 7(b), the magnetoresistance,

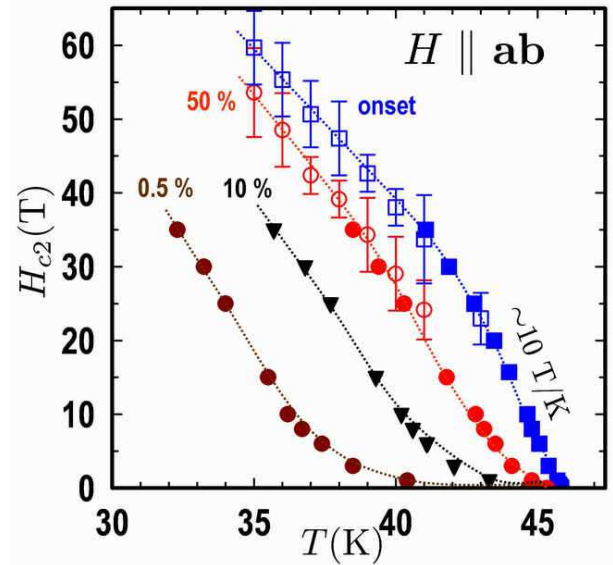


FIG. 8: Temperature dependence of the upper critical field $H_{c2}^{\parallel}(T)$ along the ab plane obtained from dc (filled symbols) and pulsed (open symbols) measurements. The data extracted from the results shown in Fig. 3, and Fig. 5, show the temperatures at which the resistance reaches 0.5 %, 10 %, 50 % of the normal state resistance, as extrapolated linearly from the $\rho_N(T, H)$ temperature dependence above $T_c(H)$. The onsets of superconducting transition were determined as shown in Fig. 4 and correspond well to the 90 % transitions. The dotted lines are guides to the eye.

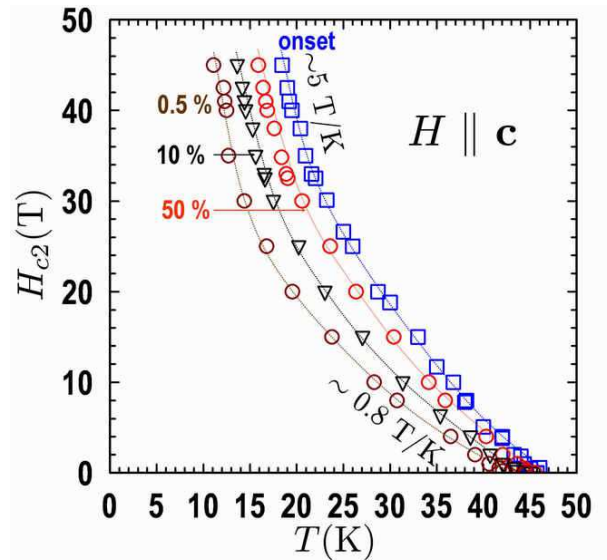


FIG. 9: Temperature dependence of the upper critical fields $H_{c2}^{\perp}(T)$ along the c -axis obtained from the dc measurements. The data extracted from the results shown in Fig. 4, and Fig. 6, show the temperatures at which the resistance reaches 0.5 %, 10 %, 50 % of the normal state resistance, as extrapolated linearly from the $\rho_N(T, H)$ temperature dependence above $T_c(H)$. The onsets of superconducting transition were determined as shown in Fig. 4 and correspond well to the 90 % transitions. The dashed lines are guides to the eye.

$(\rho_{xx}(H) - \rho_{xx}(0))/\rho_{xx}(0) \propto H^2$ for both field orientations and $H \gtrsim 15$ T exhibits a quadratic field dependence. However, if this quadratic contributions are removed, a weak remanent positive MR is observed at low fields $H \lesssim 15$ T, as shown in Fig. 7(c). This remanent MR is identical for both field orientations, which in turn suggests a spin mechanism behind this positive MR component. Interestingly, such a spin dependent positive MR is ubiquitous in diluted magnetic semiconductors (DMS) in the paramagnetic phase^{42,43,44}. It originates from the giant spin-splitting Δ_s of the electron states, which considerably affects quantum corrections to the conductivity brought about by the effect of disorder modified electron-electron interactions⁴⁵. Since Δ_s in DMSs is proportional to the magnetization M of the localized spins, this positive MR scales with B and T like the Brillouin function. Importantly, this positive MR is absent in a ferromagnetic phase, when localized moments are already aligned at $H = 0$. This mechanism can also produce MR in Nd(O,F)FeAs, provided that at least some of localized magnetic moments μ (most likely of Nd³⁺ ions with $\mu = 3.6\mu_B$) are in a paramagnetic phase. At the same time, as shown in Fig. 7(d), the Hall coefficient R_H strongly depends on H at low field. Such a dependence could also result from quantum corrections to ρ_{xy} from electron-electron interactions, but maybe a result of multiband conductivity, as well.

Based on the results shown in Figs. 8 and 9, the following points can be made:

1. The 100–200 T field scale of H_{c2} in Nd(O_{0.7}F_{0.3})FeAs is comparable to that of high- T_c cuprates.

2. $H_{c2}^\perp(T)$ perpendicular to the *ab* plane exhibits a pronounced upward curvature similar to what was first reported for polycrystalline La(O,F)FeAs⁷. This is very different from the one-band WHH behavior and appears to be an intrinsic property of oxypnictides rather than manifestations of the vortex melting or the onset of pinning at $H = H^*(T)$.

3. The slopes $H_{c2}^{\parallel} = |dH_{c2}^{\parallel}/dT|$ and $H_{c2}^{\perp} = |dH_{c2}^{\perp}/dT|$ for both field orientations increase significantly just a few Kelvins below T_c . Thus, low-field $H < 9$ T measurements may underestimate the actual values of $H_{c2}^{\perp} = \phi_0/2\pi\xi_{a0}^2T_c$ and $H_{c2}^{\parallel} = \phi_0/2\pi\xi_{a0}\xi_{c0}T_c$ at $T \approx T_c$, from which the coherence lengths $\xi_a(T) = (1 - T/T_c)^{-1/2}\xi_{a0}$ and $\xi_c(T) = (1 - T/T_c)^{-1/2}\xi_{c0}$ in the *ab* plane and along the *c*-axis can be extracted. As it is evident from Figs. 8 and 9, the high-temperature slopes H_{c2}^{\perp} and H_{c2}^{\parallel} attain different values above $\simeq 10$ T, so the use of high magnetic fields becomes decisive for revealing the true intrinsic superconducting parameters of Nd(O_{0.7}F_{0.3})FeAs single crystals. This may also explain why low-field measurements^{33,34,35} show lower values of dH_{c2}^{\parallel}/dT and dH_{c2}^{\perp}/dT .

III. THERMALLY ACTIVATED RESISTIVITY

Shown in Figs 10 and 11 are the temperature dependencies of the ohmic resistivity $\rho_{xx}(T, H)$ measured above the irreversibility field, $H^* < H < H_{c2}$ for both field orientations. These data can be described well by the Arrhenius dependence

$$\ln \rho_{xx} = \ln \rho_0 - E_a(T, H)/T, \quad (1)$$

characteristic of thermally-activated flux flow (TAFF) of vortices, which has been studied extensively on high- T_c cuprates. Here $E_a(T, B) = -\partial \ln \rho_{xx} / \partial (1/T)$ is the activation energy determined by hopping of vortex bundles in the pinning potential. Several features of the data shown in Figs. 10 and 11 should be pointed out.

1. The Arrhenius dependence holds over 4-5 decades of ρ_{xx} , down to the limit of sensitivity of our transport measurements. This indicates that thermally-activated vortex hopping in Nd(O_{0.7}F_{0.3})FeAs is similar to that of high- T_c cuprates and is much more pronounced than in lower- T_c pnictides like La(O_{1-x}F_x)FeAs. The good linear behavior evident from Figs 10 and 11 also indicates that the low-temperature dependence of $E_a(T)$ is approximately linear, $E_a(T) = E_m(1 - T/T_m)$, where T_m is a parameter with the dimensionality of temperature. In this case the term T/T_m can be eliminated by re-defining $\rho_0 \rightarrow \rho_0 \exp(E_m/T_m)$ in Eq. (1) without changing any observed characteristics.

2. The higher temperature $\log \rho_{xx}(T)$ data level off at a field independent value corresponding to the normal state resistivity ρ_n .

3. The $\log \rho_{xx}(T)$ lines for different $H||c$ extrapolate to the same temperature, $\approx T_c$, indicating that $T_m = T_c$, $\rho_0 \approx \rho_n \exp(E_m/T_c)$ and E_m is practically independent of H . However, for the parallel field orientation, this is not the case because of the field dependence of E_m , as shown below.

From the low-temperature slope of $\log \rho_{xx}$ the field dependencies of the activation energy $E_a = -d \ln \rho_{xx} / d(1/T)$ can be obtained. The results presented in Fig. 12 for both field orientations show that $E_a \simeq (3 - 4) \times 10^3$ K at low fields. The activation energy $E_a \simeq 2 \times 10^4$ K for a polycrystalline Nd(O,F)FeAs measured previously⁸ is higher than for the single crystals studied in this work (similar thermally-activated resistivity was recently observed on polycrystalline Nd(O_{0.82}F_{0.18})FeAs⁶). The field dependencies of $E_a(B)$ for $H||c$ and $H \perp c$ are also markedly different. $E_a(H)$ for $H||c$ exhibits a rather conventional field dependence characteristic of thermally-activated transport: a constant value at low fields $H < 3$ T where single-vortex pinning dominates, followed by a power law decrease $E_m \propto H^{-1.1}$ characteristic of collective creep at higher fields, $H > 3$ T⁴⁶. By contrast, the activation energy for $H||ab$ exhibits a rather weak power law decrease $E_m \propto H^{-0.17}$ in the entire field interval where $\rho_{xx}(T, H)$ was measured.

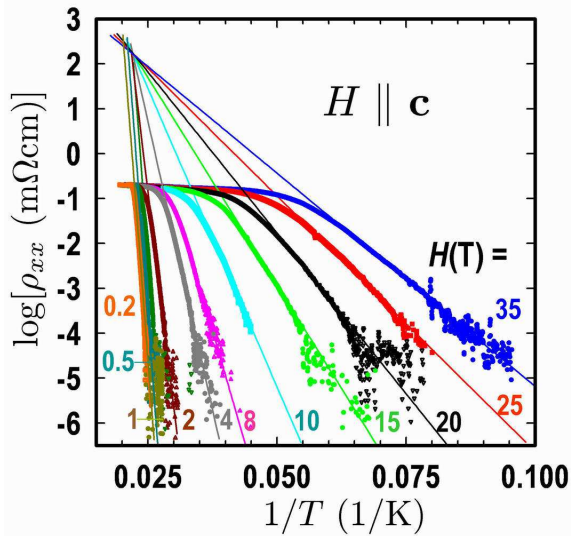


FIG. 10: Arrhenius plot for $\rho_{xx}(T)$ at different magnetic fields perpendicular to the ab plane.

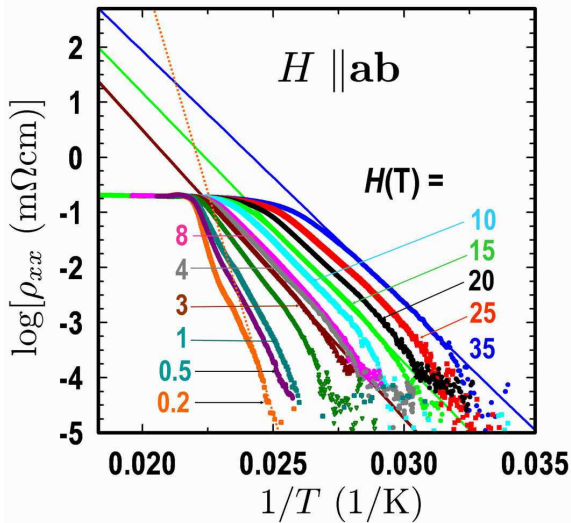


FIG. 11: Arrhenius plot for $\rho_{xx}(T)$ at different magnetic fields parallel to the ab plane.

The field and temperature dependencies of $E_a(T, H)$ can be described by the following scaling function

$$E_a = \frac{E_0(1 - T/T_c)^\alpha}{[1 + H/H_0(T)]^\beta} \left[1 - \frac{H}{H_{c2}(T)} \right]^\delta, \quad (2)$$

where H_0 quantifies the field above which vortex dynamics is determined by collective effects of vortex interaction⁴⁶. From the data presented above, we obtain $H_0 \simeq 3$ T, $\alpha \simeq 1$, and $\beta \simeq 1.1$ for $\mathbf{H} \parallel c$ and $\beta \simeq 0.17$ for $\mathbf{H} \parallel ab$.

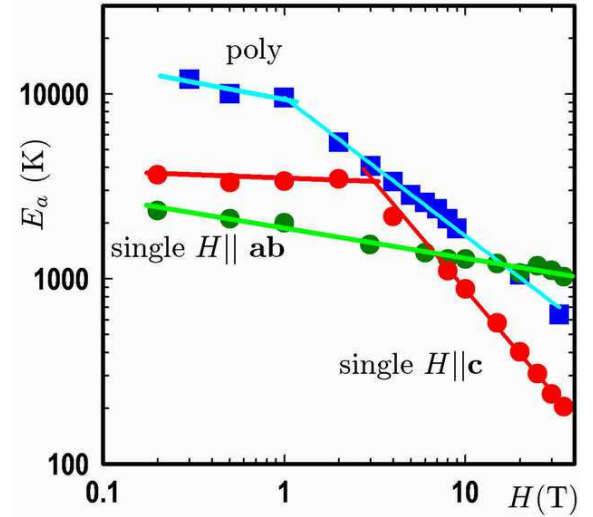


FIG. 12: Field dependencies of the activation energy $E_a(H)$ for $H \perp ab$ and $H \parallel ab$. The solid squares show the data for Nd(O,F)FeAs polycrystal measured earlier.

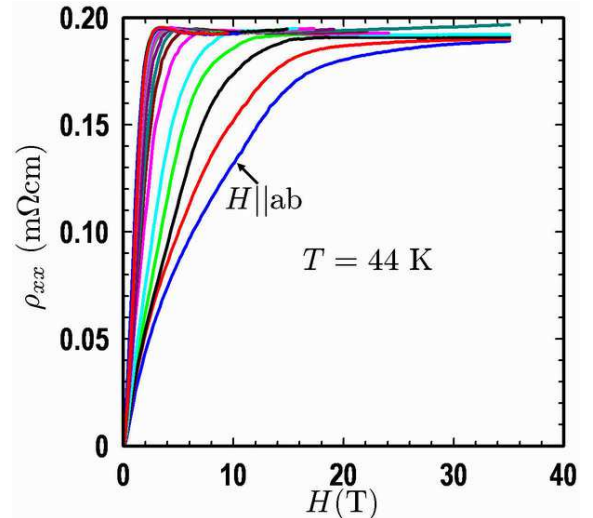


FIG. 13: The resistivities $\rho_{xx}(T, H)$ measured at 44 K for different angles θ between \mathbf{H} and the ab plane.

IV. ANGULAR DEPENDENCIES

The TAFF resistivity $\rho_{xx}(T, H, \theta)$ was measured at different angles θ between \mathbf{H} and the ab plane, as illustrated by a representative example shown in Fig. 13. The angular dependencies of $H_{c2}(\theta)$ extracted from the $\rho_{xx}(T, H, \theta)$ at 90 %, 50 %, and 10 % of $\rho_n(T, H)$ are shown in Fig. 14.

It is clearly seen that the anisotropy as $\gamma = H_{c2}^{\parallel}/H_{c2}^{\perp}$ decreases when calculated at lower resistive transitions. At the same time $H_{c2}^{90\%}(\theta)$ shown in Fig. 14 notably de-

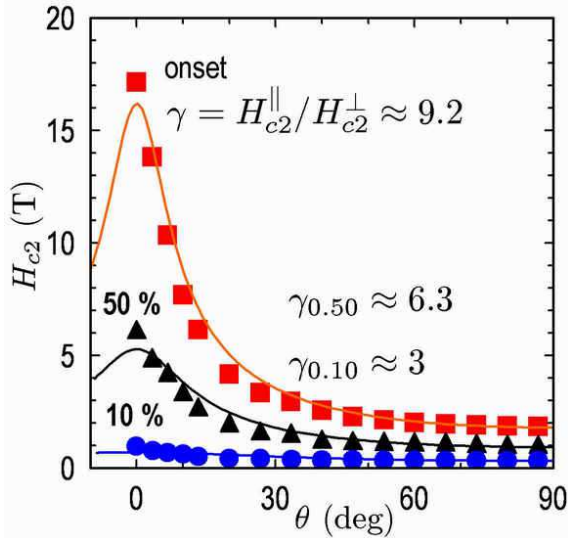


FIG. 14: Angular dependence of $H_{c2}(\theta)$ defined at $\rho_{xx} = 0.9$ 0.5 0.1 ρ_n at 44 K. The solid lines show the fits with Eq. (3).

partures from the standard Ginzburg-Landau formula:

$$H_{c2}(\theta) = \frac{H_{c2}^{\perp}}{\sqrt{\sin^2 \theta + \gamma^{-2} \cos^2 \theta}} \quad (3)$$

where $\gamma = (m_c/m_a)^{1/2}$ is defined by the ratio of effective masses along the ab plane and the c-axis. The fit to Eq. (3) yields $\gamma \approx 8.9$ in this case. Data taken at 50 % and 10 % departure from Eq. (3) even stronger, which may result from increasing contribution of TAFF transport at lower resistivities.

The temperature dependencies of $\gamma(T)$ obtained from the H_{c2} data shown in Figs. 8 and 9 for H_{10} , H_{50} and H_{c2} are shown in Fig. 15. Contrary to the standard one-band behavior, γ turns out to be temperature dependent, the values of $\gamma_{10}(T)$, $\gamma_{50}(T)$ and $\gamma(T)$ being rather different, especially just below T_c . While the parameter of H_{c2} anisotropy, $\gamma(T) = H_{c2}^{\parallel}/H_{c2}^{\perp}$ decreases from ≈ 9 at T_c to ≈ 5 at 34 K, the field H_{10} becomes more anisotropic upon decreasing T . Below $T \approx 38$ K, however, these values of $\gamma(T)$ converge.

V. H_{c2} IN TWO-BAND SUPERCONDUCTORS

To understand how different pairing scenarios could manifest themselves in the observed temperature dependencies of $H_{c2}(T)$, we use the two-band BCS theory in which T_c for interband scattering is given by^{47,48}

$$T_{c0} = \Omega \exp[-(\lambda_+ - s\lambda_0)/2w], \quad (4)$$

where $\lambda_{\pm} = \lambda_{11} \pm \lambda_{22}$, $w = \lambda_{11}\lambda_{22} - \lambda_{12}\lambda_{21}$, $s = \text{sign}(w)$, and $\lambda_0 = (\lambda_{-}^2 + 4\lambda_{12}\lambda_{21})^{1/2}$, λ_{12} and λ_{21} are pairing constants in bands 1 and 2, and λ_{12} and λ_{21} quantify

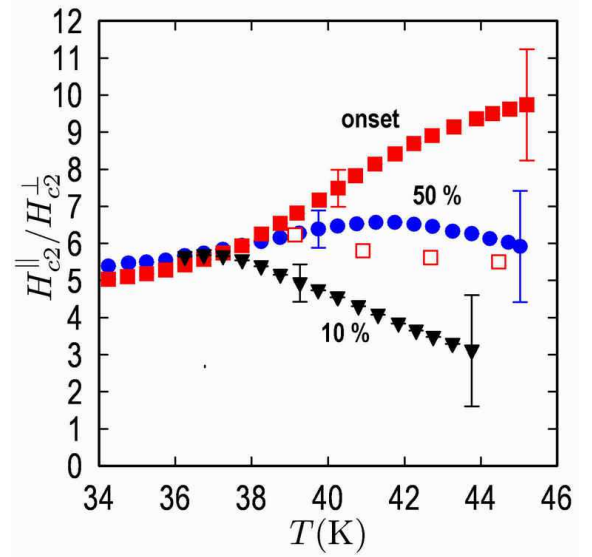


FIG. 15: Temperature dependencies of γ_{10} , γ_{50} and γ_{90} . The open squares show the data from Ref. 35 measured on Nd(O_{0.82}F_{0.18})FeAs single crystal with higher $T_c = 51.5$ K. These data are plotted at reduced temperatures.

interband coupling. For s-wave pairing, intraband impurity scattering does not affect T_{c0} , while weak interband scattering reduces T_c according to^{26,49,50}

$$T_c = T_{c0} - \frac{\pi}{8\lambda_0} [\lambda_0\gamma_+ + \lambda_-\gamma_- - 2\lambda_{21}\gamma_{12} - 2\lambda_{12}\gamma_{21}] \quad (5)$$

where $\gamma_{\pm} = \gamma_{12} \pm \gamma_{21}$, and γ_{12} and γ_{21} are scattering rates between bands 1 and 2, $N_1\gamma_{12} = N_2\gamma_{21}$ and $N_1\lambda_{12} = N_2\lambda_{21}$, where N_1 and N_2 are partial densities of states in bands 1 and 2, respectively. In the following we discuss two scenarios: 1. Conventional s-wave pairing dominated by strong intraband coupling, $w > 0$. 2. Strong interband pairing $w < 0$ which can result in the π shift between the order parameters on two bands for interband repulsion $\lambda_{12} < 0$ (s^{\pm} pairing¹⁵).

As follows from Eq. (5), interband repulsion with $\lambda_{12} < 0$ and $\lambda_{21} < 0$ enhances T_c depression due to interband impurity scattering between different pieces of the Fermi surface with opposite signs of the order parameter. This suppression may be reduced by strong coupling effects⁵¹. By contrast, for strong interband attraction, $4\lambda_{12}\lambda_{21} \gg \lambda_{-}^2$, Eq. (5) yields

$$T_c = T_{c0} - \frac{\pi\gamma_{12}}{8} \left(1 - \sqrt{\frac{N_1}{N_2}}\right)^2 \quad (6)$$

Here T_c suppression is much weaker than for the s^{\pm} pairing because the factor $(1 - \sqrt{N_1/N_2})^2$ reduces the effect of interband scattering, making T_c independent of γ_{12} in the special case of $N_1 = N_2$. For instance, for $N_1 = 1.2N_2$, Eq. (6) gives a rather weak suppression of $T_c \simeq T_{c0}(1 - 0.02g)$ even in the dirty limit, $g = \gamma_{12}/2\pi T_{c0} > 1$.

In the dirty limit, the equation for H_{c2} , which takes into account both orbital and Zeeman pairbreaking for negligible interband scattering, can be written in the following parametric form²⁶:

$$\ln t = -[U_1(h) + U_2(h) + \lambda_0/w]/2 + \quad (7)$$

$$s[(U_1(h) - U_2(h) - \lambda_-/w)^2/4 + \lambda_{12}\lambda_{21}/w^2]^{1/2},$$

$$H_{c2} = 2\phi_0 k_B T_c t h / \hbar D_0, \quad (8)$$

where $t = T/T_{c0}$, and the functions $U_{1,2}$ are defined by

$$U_{1,2}(h) = \text{Re}\psi[1/2 + (i + D_{1,2}/D_0)h] - \psi(1/2), \quad (9)$$

$\psi(x)$ is the di-gamma function, D_1 and D_2 are diffusivities in band 1 and 2, $D_0 = \hbar/2m$, and the parameter h runs from 0 to ∞ as T varies from T_c to 0. For equal diffusivities, $\eta = D_2/D_1 = 1$, and negligible Zeeman pairbreaking, $D_0 \ll D_{1,2}$, Eq. (8) simplifies to the one-band de-Gennes-Maki equation, $\ln t + U(h) = 0$. If the magnetic field H is inclined by the angle θ with respect to the ab planes, Eqs. (8)-(9) also describe the angular dependence of $H_{c2}(\theta)$ if the intraband diffusivities are replaced by their angular-dependent values:

$$D_m(\theta) = [D_m^{(a)2} \sin^2 \theta + D_m^{(a)} D_m^{(c)} \cos^2 \theta]^{1/2} \quad (10)$$

where $m = 1, 2$, and $D_m^{(a)}$ and $D_m^{(c)}$ are the in-plane and the c -axis principal values of $D_m^{\alpha\beta}$.

$H_{c2}(T)$ curves shown in Fig. 8 and 9 exhibit pronounced upward curvature for the field along the c -axis, and the downward curvature for the field along the ab plane, similar to the behavior of $H_{c2}(T)$ first observed on polycrystalline $\text{LaO}_{0.89}\text{F}_{0.11}\text{FeAs}$ ⁷. Such temperature dependence of $H_{c2}(T)$ has been often observed on MgB_2 , suggesting that the two-band theory in which two bands have different diffusivities can also be used to describe $H_{c2}(T)$ in oxypnictides (the superconducting gaps on the disconnected pieces of the Fermi surface can be either different or the same). If interband scattering is negligible, neither T_c nor H_{c2} depend on the sign of λ_{12} , so we consider two different cases: 1. dominant intraband coupling, $w = \lambda_{11}\lambda_{22} - \lambda_{12}\lambda_{21} > 0$ and 2. dominant interband coupling, $w = \lambda_{11}\lambda_{22} - \lambda_{12}\lambda_{21} < 0$.

Shown in Fig. 16(a) is an example of the fit of Eq. (8)-(9) to the data for case 1 with $\lambda_{11} = \lambda_{22} = 0.5$, and $\lambda_{12} = \lambda_{21} = 0.25$, in which case $T_c = \Omega \exp[-1/(\lambda_{11} + \lambda_{12})] = 50\text{K}$ corresponds to $\Omega \simeq 190\text{K}$. Fig. 16(a) shows the fit without taking paramagnetic effects into account for $D_2 = 0.08D_1$, which suggests that scattering in one band is significantly stronger than in the other. We do not discuss here microscopic mechanisms behind such band disparity; instead we focus on the set of parameters which fit the data and the extent to which these parameters are different for the case of $w > 0$ and $w < 0$. Extrapolations of $H_{c2}^{\parallel}(T)$ to $T = 0$ based on the observed slope at T_c suggests $H_{c2}^{\parallel}(0) \sim 220\text{T}$, well above the weak coupling BCS paramagnetic limit $H_p[\text{T}] = 1.84T_c[\text{K}] \simeq 90\text{T}$.

Fig. 16(a) shows the fit in the case of strong interband pairing $\lambda_{12}\lambda_{21} > \lambda_{11}\lambda_{21}$ for $\lambda_{11} = \lambda_{22} = 0.49$, $\lambda_{12} =$

$\lambda_{21} = 0.5$ and $D_2^a = 0.007D_1^a$. Reproducing the observed upward curvature of $H_{c2}^{\perp}(T)$ for this case requires a much greater disparity of the band diffusivities than for the previous case. Reducing λ_{11} and λ_{22} shifts the region of upward curvature to lower temperatures, which makes fitting the data even more difficult. These features may put serious constraints on the s^{\pm} pairing scenario.

Given the very high extrapolated values of $H_{c2}^{\parallel}(0)$ in Fig. 16(a), the role of paramagnetic effects becomes very important. Shown in Fig. 16(c) is the fit for the same parameters as in Fig. 16(a) but with the account of the Zeeman pairbreaking for $D_1^{(a)} = 10D_0$ and $[D_2^{(a)}D_2^{(c)}/D_1^{(a)}D_1^{(c)}]^{1/2} = 0.7D_0$. In this case the values of $H_{c2}(T)$ at low temperatures are significantly reduced as compared to what may be expected from the fit in Fig. 16(a), which ignores the paramagnetic effects.

Several remarks should be made regarding the fits in Fig. 16(a-c). First, applying weak coupling Eqs. (8)-(9) for a superconductors with $T_c = 50\text{K}$ obviously neglects the strong coupling renormalization effects of the Eliashberg theory. However given the lack of microscopic theory of superconductivity in oxypnictides, the use of the BCS-type approach may have its own merits given that the shape of the $H_{c2}(T)$ curve described by Eqs. (8)-(9) depends only on the ratio of the constants λ_{mn} but it is basically insensitive to the particular s -wave pairing mechanisms. The usual way of treating strong coupling effects in Eqs. (8)-(9) is to express them in terms of experimentally observed parameters⁵² such as T_c and D_1 and D_2 extracted from normal state transport measurements and the observed slopes dH_{c2}/dT . The second remark is that the actual paramagnetic limit $H_p \simeq (1 + \lambda)H_p^{BCS}$ is significantly enhanced by strong coupling effects as compared to the BCS value⁵³. Here $\lambda \sim 1$ is a characteristic bare coupling constant for the relevant exchange boson, so $H_{c2}(T)$ values may significantly exceed H_p^{BCS} as has been observed in other superconductors, for example PbMo_6S_8 ^{54,55}. Thus, Eqs. (8)-(9) may capture the qualitative behavior of $H_{c2}(T)$ as functions of materials parameters if they are expressed in terms of the observed quantities, and the Zeeman terms are renormalized by strong coupling effects.

VI. DISCUSSION

Our high-field data obtained on a $\text{Nd}(\text{O}_{1-x}\text{F}_x)\text{FeAs}$ single crystals show extremely high H_{c2} values, consistent with previous low-field measurements on single crystals^{3,33,34,35,36} and high-field measurements on polycrystals^{7,8}. Our values of the temperature-dependent H_{c2} slopes, $H_{c2}^{\parallel} \approx 8 - 10\text{ T/K}$ and $H_{c2}^{\perp} \approx 1.2 - 5\text{ T/K}$ measured from the resistivity onset of superconductivity are considerably higher than the values of H_{c2} extracted from calorimetry measurements on $\text{Nd}(\text{O}_{1-x}\text{F}_x)\text{FeAs}$ single crystals³⁶, which may be affected by strong paramagnetism of Nd^{3+} ions at high

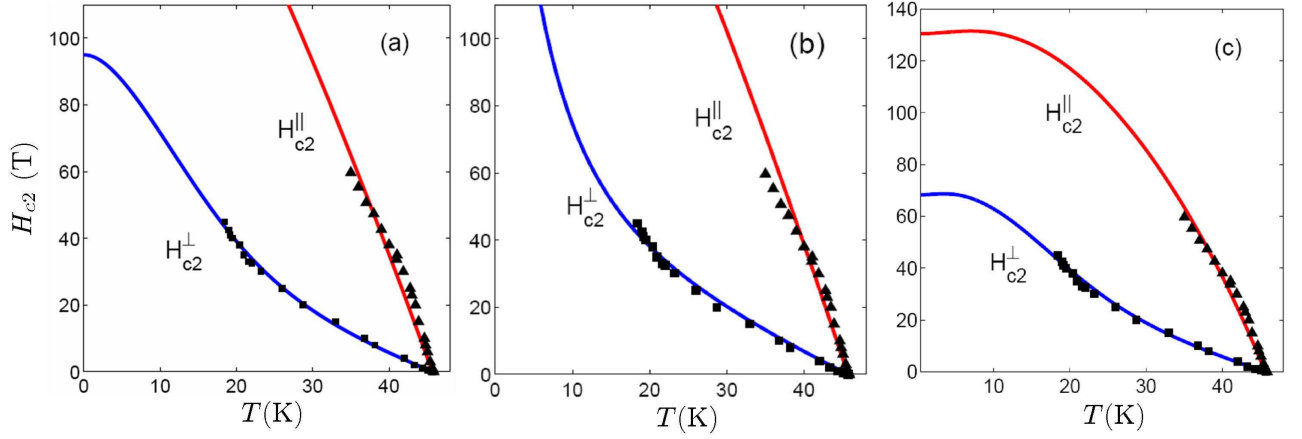


FIG. 16: Fits of Eqs. (8)-(9) to the experimental data shown in Figs. 8 and 9 for different pairing scenarios: $w > 0$, $\lambda_{11} = \lambda_{22} = 0.5$, $\lambda_{12} = \lambda_{21} = 0.25$, $\eta_{\perp} = D_2^{(a)}/D_1^{(b)} = 0.08$, $\eta_{\parallel} = [D_2^{(a)}D_2^{(c)}/D_1^{(a)}D_1^{(c)}]^{1/2} = 1$, and negligible paramagnetic effects (a); $w < 0$, $\lambda_{11} = \lambda_{22} = 0.49$, $\lambda_{12} = \lambda_{21} = 0.5$, $\eta_{\perp} = D_2^{(a)}/D_1^{(b)} = 0.007$, $\eta_{\parallel} = [D_2^{(a)}D_2^{(c)}/D_1^{(a)}D_1^{(c)}]^{1/2} = 1$, and negligible paramagnetic effects (b); $w > 0$, $\lambda_{11} = \lambda_{22} = 0.5$, $\lambda_{12} = \lambda_{21} = 0.25$, $\eta_{\perp} = D_2^{(a)}/D_1^{(b)} = 0.08$, $\eta_{\parallel} = [D_2^{(a)}D_2^{(c)}/D_1^{(a)}D_1^{(c)}]^{1/2} = 1$, $d_{\perp} = D_1^{(a)}/D_0 = 10$, and $d_{\parallel} = [D_2^{(a)}D_2^{(c)}/D_1^{(a)}D_1^{(c)}]^{1/2}/D_0 = 0.7$ (c).

fields¹⁰. We should also mention several issues, which may complicate accurate extraction of the anisotropy in Nd(O_{1-x}F_x)FeAs single crystals grown by the flux method, which usually results in intergrowths and stacking faults parallel to the ab plane. Such planar defects may increase the apparent anisotropy parameter γ and give rise to the local modulations of order parameter along the c-axis. The latter may broaden the resistive transition at T_c and the upward curvature of $H_{c2}(T)$ near T_c , which could mask the two-band effects.

Because of very high values of H_{c2}^{\parallel} and H_{c2}^{\perp} , our high field measurements up to 60 T are still mostly limited to the temperatures not too far from T_c , particularly for the field parallel to the ab plane. As a result, it is hard to unambiguously evaluate the values $H_{c2}(0)$, as Figs. 16(a-c) illustrate. Yet we can evaluate the in-plane and the c-axis GL coherence lengths, $\xi_a = (\phi_0/2\pi H_{c2}^{\perp} T_c)^{1/2} \simeq 2.3$ nm and $\xi_c = \xi_a/\gamma = 0.26$ nm for $\gamma = 9$, $H_{c2\perp}^{\perp} = 1.2$ T/K and $T_c = 50$ K. These values of ξ_a and ξ_c are not too different from those for YBa₂Cu₃O_{7-x}. The fits shown in Figs. 16(a-c) also indicate the importance of paramagnetic effects in $H_{c2}(T)$, particularly the fact that extrapolations of H_{c2} to low temperatures based on the measured slope H_{c2}' and the WHH formula $H_{c2} \simeq 0.7T_c H_{c2}'^5$ may grossly overestimate $H_{c2}(0)$. At the same time, the importance of paramagnetic effects in oxypnictides might open up possibilities of observing first order phase transitions or perhaps the Fulde-Ferrel-Larkin-Ovchinnikov inhomogeneous states at very high magnetic fields.

The temperature dependence of $H_{c2}^{\perp}(T)$ shown in Fig. 9 is rather different from the conventional one-band WHH behavior, which may be characteristic of many oxypnictides. This confirms our earlier qualitative conclusion inferred from indirect measurements of $H_{c2}^{\perp}(T)$ on polycrystalline oxypnictides⁷. One possibility to explain the

significant upward curvature of $H_{c2}^{\perp}(T)$ is based on the two-band model. This conclusion is also consistent with the temperature dependent mass anisotropy parameter, $\gamma(T)$, reminiscent of the behavior of MgB₂^{26,56}. Yet many important points remains controversial. First, to explain the observed upward curvature of $H_{c2}^{\perp}(T)$, we had to assume a rather high difference in the intraband diffusivities, $D_2 \sim (0.1 - 0.01)D_1$ (depending on the pairing scenario), considerably higher than the effective mass difference for Γ and M electron pockets predicted by ab-initio calculations^{16,17,18,19}. One has therefore to assume that scattering on impurities or strong magnetic excitations may produce such big differences in D_1 and D_2 .

Our data enable us to make further qualitative conclusions regarding the s-wave two-band pairing scenarios with and without the interband π shift. The first one is less susceptible to the pairbreaking effect of interband impurity scattering, as follows from Eqs. (5) and (6). Indeed, the fact that our Nd(O,F)FeAs single crystal has the same T_c as sintered multiphase polycrystals, seems to suggest that the impurity scattering does not suppress T_c much. The latter may also indicate that oxypnictides are effectively in the clean limit just because of their short coherence lengths, $\xi_a < \ell$, where ℓ is the mean free path. Yet s^{\pm} pairing is certainly more susceptible to the pairbreaking interband impurity scattering. Another indication that the s-wave pairing without the interband π shift appears to fit our data better comes from the fact that, in order to explain the observed upward curvature of $H_{c2}^{\perp}(T)$ in Fig. 16(b) in the s^{\pm} model, we have to assume the ratio D_1/D_2 to be about an order of magnitude smaller than $D_2/D_1 \sim 0.1$ required for the more traditional model of strong intraband pairing and weaker interband pairing. These constraints may reduce the number of possible scenarios of superconductivity in

the oxypnictides.

As far as vortex dynamics in Nb(F,O)FeAs is concerned, our data presented in Figs. 3 and 4 show that high magnetic fields parallel to the c-axis mostly shift the resistive transition without significant broadening of the $\rho_{xx}(T)$ curves, while H parallel to the ab plane changes the shape of $\rho_{xx}(T)$, but certainly not as strong as for high- T_c cuprates⁴⁶. This suggests that despite the rather high values of γ , thermal fluctuation of vortices in Nb(F,O)FeAs single crystals are weaker than in most anisotropic layered cuprates, like Bi-2212. This conclusion is consistent with the data of other groups⁵⁷ and with the relatively high activation energy $E_0 \sim 3 \times 10^3$ K extracted from our transport measurements. The effect of thermal fluctuations is also quantified by the Ginzburg parameter, $Gi = (2\pi k_B T_c \mu_0 \Lambda_0^2 / \phi_0^2 \xi_c)^2 / 2$, where Λ_0 is the in-plane London penetration depth. Taking $\Lambda_0 = 200$ nm, $\xi_c = 0.26$ nm and $T_c = 49$ K, we obtain $Gi \simeq 10^{-2}$, of the order of the typical Ginzburg number for YBCO.

For two-band superconductors, the above estimates of Gi remain qualitatively the same if γ and ξ are taken for the band with the minimum effective mass or maximum electron mobility²⁶. By contrast, Gi in La(O,F)FeAs is close to Gi in MgB₂, about 30 times smaller than Gi in Nd(O,F)FeAs^{7,8}.

In conclusion, our high-field magneto-transport measurements on single crystal Nd(O_{0.70}F_{0.30})FeAs have revealed very high upper critical fields and their anomalous temperature dependencies. We also observe a pronounced thermally-activated flux flow resistivity which may indicate rich vortex dynamics in single layer oxypnictides.

The work at NHMFL was supported by the NSF Cooperative Agreement No. DMR-0084173, by the State of Florida, by the DOE, by the NHMFL IHRP program (FH), and by AFOSR grant FA9550-06-1-0474 (AG and DCL).

-
- ¹ Y. Kamihara, T. Watanabe, M. Hirano, and H. Hosono. *J. Am. Chem. Soc.* **130**, 3296 (2008).
- ² H. Takahashi, K. Igawa, K. Arii, Y. Kamihara, M. Hirano, and H. Hosono. *Nature* **453**, 376 (2008).
- ³ C. Martin, R. T. Gordon, M. A. Tanatar, M. D. Vannette, M. E. Tillman, E. D. Mun, P. C. Canfield, V. G. Kogan, G. D. Samolyuk, J. Schmalian, et al. (2008), arXiv.org:0807.0876.
- ⁴ J. D. Moore, K. Morrison, K. A. Yates, A. D. Caplin, Y. Yeshurun, L. F. Cohen, J. M. Perkins, C. M. McGilvery, D. W. McComb, Z. A. Ren, et al. *Supercond. Sci. Technol.* **21**, 092004 (2008).
- ⁵ C. Senatore, R. Flükiger, M. Cantoni, G. Wu, R. H. Liu, and X. H. Chen. *Phys. Rev. B* **78**, 054514 (2008).
- ⁶ X. L. Wang, S. R. Ghorbani, S. X. Dou, X.-L. Shen, W. Yi, Z.-C. Li, and Z.-A. Ren (2008), arXiv.org:0806.1318, unpublished.
- ⁷ F. Hunte, J. Jaroszynski, A. Gurevich, D. C. Larbalestier, R. Jin, A. S. Sefat, M. A. McGuire, B. C. Sales, D. K. Christen, and D. Mandrus. *Nature* **453**, 903 (2008).
- ⁸ J. Jaroszynski, S. C. Riggs, F. Hunte, A. Gurevich, D. C. Larbalestier, G. S. Beobinger, F. F. Balakirev, A. Migliori, Z. A. Ren, W. Lu, et al. *Physical Review B* **78**, 064511 (2008).
- ⁹ T. Yildirim. *Phys. Rev. Lett.* **101** (2008).
- ¹⁰ C. Tarantini, A. Gurevich, D. C. Larbalestier, Z. A. Ren, X. L. Dong, W. Lu, and Z. X. Zhao (2008), arXiv.org:0805.4445, unpublished.
- ¹¹ J. Wu, P. Phillips, and A. H. C. Neto. *Phys. Rev. Lett.* **101**, 126401 (2008).
- ¹² A. Yamamoto, J. Jiang, C. Tarantini, N. Craig, A. A. Polyanskii, F. Kametani, F. Hunte, J. Jaroszynski, E. E. Hellstrom, D. C. Larbalestier, et al. *Appl. Phys. Lett.* **92**, 252501 (2008).
- ¹³ A. Yamamoto, A. Polyanskii, J. Jiang, F. Kametani, C. Tarantini, F. Hunte, J. Jaroszynski, E. Hellstrom, P. Lee, A. Gurevich, et al. *Superconductor Science and Technology* **21**, 095008 (2008).
- ¹⁴ R. Prozorov, M. E. Tillman, E. D. Mun, and P. C. Canfield (2008), arXiv.org:0805.2783, unpublished.
- ¹⁵ I. I. Mazin, D. J. Singh, M. D. Johannes, and M. H. Du. *Phys. Rev. Lett.* **101**, 057003 (2008).
- ¹⁶ D. J. Singh and M. H. Du. *Phys. Rev. Lett.* **100** (2008).
- ¹⁷ S. Raghu, X.-L. Qi, C.-X. Liu, D. J. Scalapino, and S.-C. Zhang. *Phys. Rev. B* **77**, 220503 (2008).
- ¹⁸ S. Graser, G. R. Boyd, C. Cao, H.-P. Cheng, P. J. Hirschfeld, and D. J. Scalapino. *Phys. Rev. B* **77**, 180514 (2008).
- ¹⁹ S. Ishibashi, K. Terakura, and H. Hosono. *J. Phys. Soc. Jap.* **77**, 053709 (2008).
- ²⁰ R. H. T. Wilke, S. L. Bud'ko, P. C. Canfield, D. K. Finnemore, R. J. Suplinskas, and S. T. Hannahs. *Phys. Rev. Lett.* **92**, 217003 (2004).
- ²¹ L. Lyard, P. Szabó, T. Klein, J. Marcus, C. Marcenat, K. H. Kim, B. W. Kang, H. S. Lee, and S. I. Lee. *Phys. Rev. Lett.* **92**, 057001 (2004).
- ²² A. Rydh, U. Welp, A. E. Koshelev, W. K. Kwok, G. W. Crabtree, R. Brusetti, L. Lyard, T. Klein, C. Marcenat, B. Kang, et al. *Phys. Rev. B* **70**, 132503 (2004).
- ²³ V. Braccini, A. Gurevich, J. E. Giencke, M. C. Jewell, C. B. Eom, D. C. Larbalestier, A. Pogrebniyakov, Y. Cui, B. T. Liu, Y. F. Hu, et al. *Phys. Rev. B* **71**, 012504 (2005).
- ²⁴ M. Angst, S. L. Bud'ko, R. H. T. Wilke, and P. C. Canfield. *Phys. Rev. B* **71**, 144512 (2005).
- ²⁵ H.-J. Kim, H.-S. Lee, B. Kang, W.-H. Yim, Y. Jo, M.-H. Jung, and S.-I. Lee. *Phys. Rev. B* **73**, 064520 (pages 5) (2006).
- ²⁶ A. Gurevich. *Physica C* **456**, 160 (2007), *phys. Rev. B* **67**, 184515 (2003).
- ²⁷ S. L. Bud'ko and P. C. Canfield. *Phys. Rev. B* **65**, 212501 (2002), S.L. Bud'ko, P.C. Canfield, V.G. Kogan. *Physica C* **387**, 85 (2002).
- ²⁸ V. Ferrando, P. Manfrinetti, D. Marré, M. Putti, I. Sheikin, C. Tarantini, and C. Ferdeghini. *Phys. Rev. B* **68**, 094517 (2003).
- ²⁹ E. Ohmichi, T. Masui, S. Lee, S. Tajima, and T. Osada. *J. Phys. Soc. Japan* **73**, 2065 (2004).
- ³⁰ A. Gurevich, S. Patnaik, V. Braccini, K. H. Kim,

- C. Mielke, X. Song, L. D. Cooley, S. D. Bu, D. M. Kim, J. H. Choi, et al. *Supercond. Sci. Technol.* **17**, 278 (2004).
- ³¹ A. V. Pogrebnyakov, X. X. Xi, J. M. Redwing, V. Vaithyanathan, D. G. Schlom, A. Soukiassian, S. B. Mi, C. L. Jia, J. E. Giencke, C. B. Eom, et al. *Appl. Phys. Lett.* **85**, 2017 (2004).
- ³² P. S. P. Samuely, Z. Holanova, S. Budko, and P. Canfield. *Physica C* **435**, 71 (1959).
- ³³ Y. Jia, P. Cheng, L. Fang, H. Luo, H. Yang, C. Ren, L. Shan, C. Gu, and H.-H. Wen. *Applied Physics Letters* **93**, 032503 (2008).
- ³⁴ P. Cheng, H. Yang, Y. Jia, L. Fang, X. Zhu, G. Mu, and H.-H. Wen (2008), arXiv.org:0806.1668, unpublished.
- ³⁵ Y. Jia, P. Cheng, L. Fang, H. Yang, C. Ren, L. Shan, C.-Z. Gu, and H.-H. Wen. *Supercond. Sci. Technol.* p. 105018 (2008).
- ³⁶ U. Welp, R. Xie, A. E. Koshelev, W. K. Kwok, P. Cheng, L. Fang, and H. H. Wen (2008), arXiv.org:0807.4196, unpublished.
- ³⁷ N. R. Werthamer, E. Helfand, and P. C. Hohenberg. *Phys. Rev.* **147**, 295 (1966).
- ³⁸ P. Lindqvist, A. Nordström, and O. Rapp. *Phys. Rev. Lett.* **64**, 2941 (1990), *Phys. Rev. B* **45**, 12577–12579 (1992).
- ³⁹ P. Santhanam, C. C. Chi, S. J. Wind, M. J. Brady, and J. J. Bucchignano. *Phys. Rev. Lett.* **66**, 2254 (1991).
- ⁴⁰ C. Strunk, V. Bruyndoncx, C. Van Haesendonck, V. V. Moshchalkov, Y. Bruynseraede, C.-J. Chien, B. Burk, and V. Chandrasekhar. *Phys. Rev. B* **57**, 10854 (1998).
- ⁴¹ R. Vaglio, C. Attanasio, L. Maritato, and A. Ruosi. *Phys. Rev. B* **47**, 15302 (1993), C. Attanasio, S. Barbenera, T. Di Luccio, S.L. Prischepa, R. Russo, M. Salvato, and L. Maritato, *J. Phys. Cond. Mat.* **13**, 3215 (2001).
- ⁴² M. Sawicki, T. Dietl, J. Kossut, J. Igalson, T. Wojtowicz, and W. Plesiewicz. *Phys. Rev. Lett.* **56**, 508 (1986).
- ⁴³ I. P. Smorchkova, N. Samarth, J. M. Kikkawa, and D. D. Awschalom. *Phys. Rev. Lett.* **78**, 3571 (1997).
- ⁴⁴ T. Andrearczyk, J. Jaroszyński, G. Grabecki, T. Dietl, T. Fukumura, and M. Kawasaki. *Phys. Rev. B* **72**, 121309 (2005).
- ⁴⁵ B. L. Al'tshuler and A. G. Aronov, in *Electron-Electron Interactions in Disordered Systems*, edited by A. L. Efros and M. Pollak (North Holland, Amsterdam, 1985), p. 1, H. Fukuyama, *ibid*, p. 155; P. A. Lee and T. V. Ramakrishnan, *Rev. Mod. Phys.* **57**, 287 (1985).
- ⁴⁶ G. Blatter, M. V. Feigel'man, V. B. Geshkenbein, A. I. Larkin, and V. M. Vinokur. *Rev. Mod. Phys.* **66**, 1125 (1994).
- ⁴⁷ H. Suhl, B. T. Matthias, and L. R. Walker. *Phys. Rev. Lett.* **3**, 552 (1959).
- ⁴⁸ V. Moskalenko. *Fiz. Met. Metalloved.* **8**, 503 (1959), [*Sov. Phys. Met. Metallog.* **8**, 25 (1959)].
- ⁴⁹ A. A. Golubov and I. I. Mazin. *Phys. Rev. B* **55**, 15146 (1997).
- ⁵⁰ N. Schophol and K. Scharnberg. *Solid State Comm.* **22**, 371 (1977).
- ⁵¹ Y. Senga and H. Kontani (2008), arXiv.org:0809.0374, unpublished.
- ⁵² J. A. X. Alexander, T. P. Orlando, D. Rainer, and P. M. Tedrow. *Phys. Rev. B* **31**, 5811 (1985).
- ⁵³ M. Schossmann and J. P. Carbotte. *Phys. Rev. B* **39**, 4210 (1989).
- ⁵⁴ Ø. Fisher. *Appl. Phys.* **16**, 1 (1978).
- ⁵⁵ H. J. Niu and D. P. Hampshire. *Phys. Rev. B* **69**, 174503 (2004).
- ⁵⁶ P. Canfield, S. Bud'ko, and D. Finnemore. *Physica C* **385**, 1 (2003).
- ⁵⁷ H. Yang, C. Ren, L. Shan, and H.-H. Wen. *Phys. Rev. B* **78**, 092504 (2008).